Title

Tuning the charge blocking layer to enhance photomultiplication in organic shortwave infrared photodetectors

Journal

Journal of Materials Chemistry C, 8(43)

ISSN

2050-7526

Authors

Li, Ning
Lim, Jasmine
Azoulay, Jason D
et al.

Publication Date

2020-11-12

DOI

10.1039/d0tc03013a

Peer reviewed

Journal of Materials Chemistry C

ROYAL SOCIETY OF CHEMISTRY

PAPER

View Article Online
View Journal

Cite this: DOI: 10.1039/d0tc03013a

Tuning the charge blocking layer to enhance photomultiplication in organic shortwave infrared photodetectors

Ning Li,[a] Jasmine Lim,[b] Jason D. Azoulay[b] and Tse Nga Ng*[a]

Received 25th June 2020,
Accepted 23rd July 2020

DOI: 10.1039/d0tc03013a

rsc.li/materials-c

Emerging infrared photodetectors have reported a high level of gain using trap-assisted photomultiplication mechanisms enabling significant enhancements in their sensitivity. This work investigates a series of interfacial materials in order to understand how charge blocking layers facilitate trap-assisted photomultiplication in organic shortwave infrared detectors. The hole blocking layers induce accumulation of photogenerated holes at the interface, which in turn lowers the electron injection barrier and enables photomultiplication. In addition to examining photoresponse characteristics, the device dark current is analyzed by fitting to a charge injection model to quantify injection barriers. This demonstrates that the electric field induced barrier lowering effect plateaus with increasing applied bias. Among the interfaces studied, the best detectivity is observed using the hole blocking layer bathophenanthroline (Bphen), which reduces the probability of recombination and extends the lifetime of trapped holes to increase photomultiplication. This leads to a responsivity of 5.6 A W^{-1} (equivalent external quantum efficiency = 660% at 1050 nm) and detectivity of 10^9 Jones with broadband operation from 600 nm to 1400 nm.

Introduction

The applications of infrared detectors are wide ranging[1] and photodetectors spanning the shortwave infrared (SWIR, wavelengths of 1–3 μm) are important in many emerging technologies such as those related to imaging and biomedicine.[2–5] Conventional SWIR devices require complex fabrication processes, cooling, and are cost prohibitive for many applications. This has motivated the development of photodetectors based on organic semiconductors,[6–9] which offer advantages such as low-temperature processing, mechanical flexibility, and scalability over large areas. However, organic SWIR devices are a nascent technology that still require further improvements in photoresponse and noise reduction in order to compete with established semiconductor technologies. In particular, for SWIR detectors based on organic materials, the dissociation of excitons becomes increasingly difficult as the bandgap is narrowed due to the low dielectric polarization in organics[10,11] and high probability of recombination.[12] While operating these devices under an applied bias increases exciton dissociation efficiency,[13] this typically results in a concomitant increase in the noise current. As such, the trade-off results in no improvement in the signal-to-noise ratio. To suppress dark current under an applied bias, charge blocking layers[14] have been incorporated in organic photodiodes that operate in the visible; however, this has not been carried out for devices that operate in the SWIR.

The role of the interfacial materials adjacent to the electrodes is not limited to tuning the dark current but can also affect the device photoresponse; for example, the efficient collection of photogenerated charges depends on the interfacial barrier. Nonetheless, a delay in collecting photogenerated carriers is not necessarily detrimental, and in fact, has been leveraged to achieve trap-assisted photomultiplication[14–20] that significantly increases photocurrent. This mechanism enables multiple charges to contribute to the photo-signal for each photon absorbed. Specifically, trapping of photogenerated charges can induce band bending, which lowers injection barriers and facilitates the injection of opposite charge carriers into the device. These extra injected charges are supplied by the circuit external to the device and enable external quantum efficiencies over 100%.[15–17,20]

Trap-assisted photomultiplication has been demonstrated in visible wavelength organic photodetectors through tuning the ratio of donor and acceptor in the bulk heterojunction (BHJ) layer.[14–17,21] For example, when the BHJ blend was adjusted to a high ratio of 100 : 1 in the donor-to-acceptor content,

[a] Department of Electrical and Computer Engineering, University of California San Diego, 9500 Gilman Drive, La Jolla, CA 92093-0407, USA. E-mail: tnn046@ucsd.edu

[b] Center for Optoelectronic Materials and Devices, School of Polymer Science and Engineering, The University of Southern Mississippi, 118 College Drive #5050, Hattiesburg, MS 39406, USA

the acceptor forms isolated domains that serve as trap sites within the BHJ. Alternatively, traps near the electrode interfaces can be created by using charge blocking layers in BHJs with more conventional 1 : 2 donor-to-acceptor ratios.[19,22]

In this work, we build on the latter approach of using charge blocking layers to enhance trap-assisted photomultiplication while using a conventional BHJ ratio of 1 : 2. Unlike large bandgap BHJs, charge dissociation between donor and acceptor components in SWIR BHJs is shown to be very inefficient, if the donor-to-acceptor ratio is highly unbalanced. Moreover, there is a need to understand how varying the energy levels of charge blocking layers affects photomultiplication. Thus, this study examines interfacial layers comprised of four different materials. In place of the typical hole-transporting layer molybdenum oxide (MoO_x) used in the reference device, we compared interfacial layers consisting of zinc oxide (ZnO), bathophenanthroline (Bphen), and with direct contact to Al, and examined the resulting photocurrent and dark current. The dark current was fit to the charge injection model in ref. 23 in order to quantify the magnitude of the injection barrier and electric-field-induced barrier lowering. These analyses explain the working mechanism of photomultiplication, relate device performance to material choices and device structure, and aid in the future design and optimization of organic SWIR photodetectors.

Experimental

The molecular structures of the polymer donor and fullerene-derivative acceptor are shown in Fig. 1a. The narrow bandgap polymer showed an absorption maximum (λ_{max}) of 1050 nm, while the acceptor absorption mainly spans the visible and tails into the near infrared (Fig. 1b). The visible absorption is mainly due to the fullerene acceptor, while the donor contributes to the infrared response. A cross-sectional view of the photodetector structure is shown in Fig. 1c. We utilized different materials for the interfacial layers comprised of molybdenum oxide (MoO_x), zinc oxide (ZnO), or bathophenanthroline (Bphen), while keeping all other layers the same. In one device, no interfacial layer was utilized and the BHJ was in direct contact with the Al electrode. Fig. 1d summarizes the energy levels of the materials used in this work, and the values denote the lowest unoccupied molecular orbital (LUMO) and highest occupied molecular orbital (HOMO). The available energy states[24,25] in MoO_x are represented by the green bands, and the bandgaps of the other semiconductors are indicated by the rectangular boxes in Fig. 1. The energy diagram is drawn this way to emphasize that MoO_x is often used as a hole transporting layer, and MoO_x has available states that extend over the entire bandgaps of the BHJ materials. In contrast, ZnO and Bphen semiconductors are hole blocking layers due to their bandgap levels.

Materials

The donor polymer (poly(4-(5-(4-(3,5-bis(dodecyloxy)benzylidene)-4*H*-cyclopenta[2,1-*b*:3,4-*b*′]dithiophen-2-yl)thiophen-2-yl)-6,7-dioctyl-9-(thiophen-2-yl)-[1,2,5]thiadiazolo[3,4-*g*]quinoxaline)) was synthesized as described previously.[11,26] The acceptor [6,6]-Phenyl-*C*71-butyric acid methyl ester ($PC_{71}BM$) was purchased from Ossila Ltd. The donor and acceptor were blended at a weight ratio of 1 : 2 and dissolved in dichlorobenzene at a concentration of 24 mg mL^{-1}. The additive 1,8-diiodooctane at a 3% volume ratio was added to the semiconductor blend. The blend solution was stirred at 70 °C overnight before use. For the ZnO layer on top of the indium tin oxide (ITO) electrode, the ZnO precursor was formulated[27] by dissolving zinc acetate in a mixture of 2-ethanolamine and methoxyethanol. The precursor was stirred for 3 hours before use. For spin-coating over the BHJ, the ZnO nanoparticle solution was prepared in methanol using the procedures in ref. 28. Reagents, unless otherwise specified, were purchased from Sigma-Aldrich and used as received.

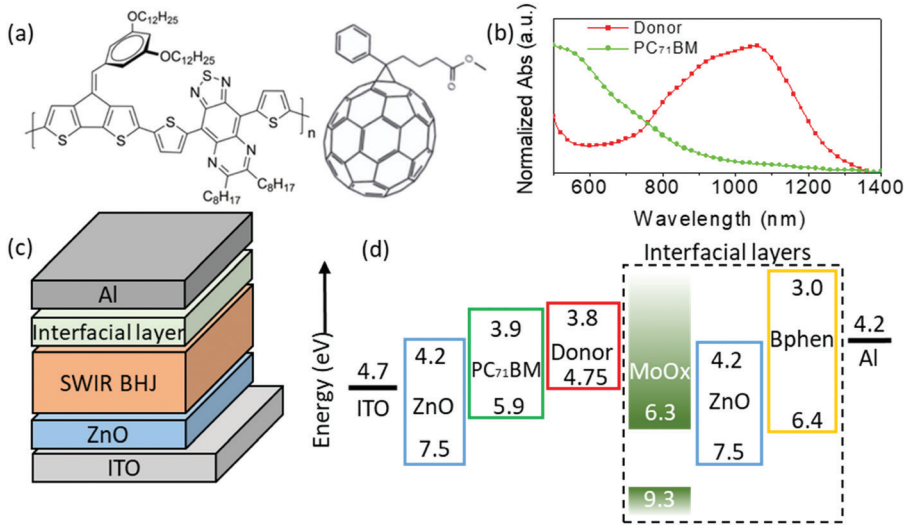

Fig. 1 (a) Chemical structures of the donor and the acceptor. (b) Normalized absorbance *versus* wavelength. (c) A cross-sectional schematic of the device structure. (d) Energy levels of the materials used in this work.

Device fabrication

The ITO substrates (sheet resistance ~ 15 Ω sq^{-1}) were ultrasonically cleaned in detergent, deionized water, acetone, and isopropanol, each for 10 min. The ZnO layer was prepared by spin-coating the ZnO precursor and annealing at 400 °C for 20 min in ambient conditions, resulting in a thin film of ~40 nm. The substrates were then transferred to a nitrogen-filled glovebox for deposition of the BHJ layer. The thickness of the spin-coated BHJ layer was measured to be ~200 nm. The interfacial layer on top of the BHJ was deposited, either by spin-coating the ZnO nanoparticle solution to form a ~15 nm film, or by evaporating 20 nm of MoO_x or Bphen. Subsequently, the devices were completed by evaporating 100 nm Al through a shadow mask, defining an active area of 0.09 cm^2. All the devices were encapsulated for characterization in air.

Device characterization

For current–voltage measurements, the voltage was provided by a Keithley (2400) sourcemeter and the current was recorded using the same sourcemeter. SWIR light was supplied by a light emitting diode (LED) (Thorlabs LED1050L) with a peak wavelength of 1050 nm. The light intensity was calibrated using a Ge detector (Newport 818IR). The device external quantum efficiency was measured under a monochromatic light source modulated at 12 Hz using an optical chopper. A low-noise current preamplifier (SR570) was used to apply voltage and amplify the device current. The amplified current was measured using a lock-in amplifier (SRS 510). To measure the noise spectra, the devices were kept in the dark, and the noise current was amplified through an SR570 preamplifier and then measured using a lock-in amplifier. The external frequency reference for the lock-in amplifier was provided by a function generator (Keysight 33500B). Lastly, the transient photoresponse was taken under irradiation with a 940 nm LED light source (Thorlabs LED940E) modulated at 100 Hz and recorded using an oscilloscope (Rigol DS1054).

Charge injection modeling

The modeling of charge injection was performed using MATLAB. The volume density of molecular sites[29] (N_{inj}) was set at 10^{27} m^{-3}. For the BHJ used in this work, the width of the Gaussian distribution σ was set at 50 meV, and the mobility was set at $\mu_0 = 10^{-3}$ cm^2 V^{-1} s^{-1}, based on ref. 30 and 11, respectively.

Results and discussion

Effect of the interfacial layer on the photocurrent

Fig. 2 shows the current–voltage characteristics of the four photodetectors, each with a different interfacial layer. The devices were measured in the dark and under illumination from a 1050 nm LED at an intensity of 4.5 mW cm^{-2}. For the structure with MoO_x, the MoO_x layer was a hole extraction interface, and negative voltage was applied to the Al electrode to reverse bias the device in Fig. 2a. For the other three devices in Fig. 2b–d, the work functions of the electrode materials dictated the charge injection barriers, and negative voltage was applied to the ITO electrode for reverse bias.

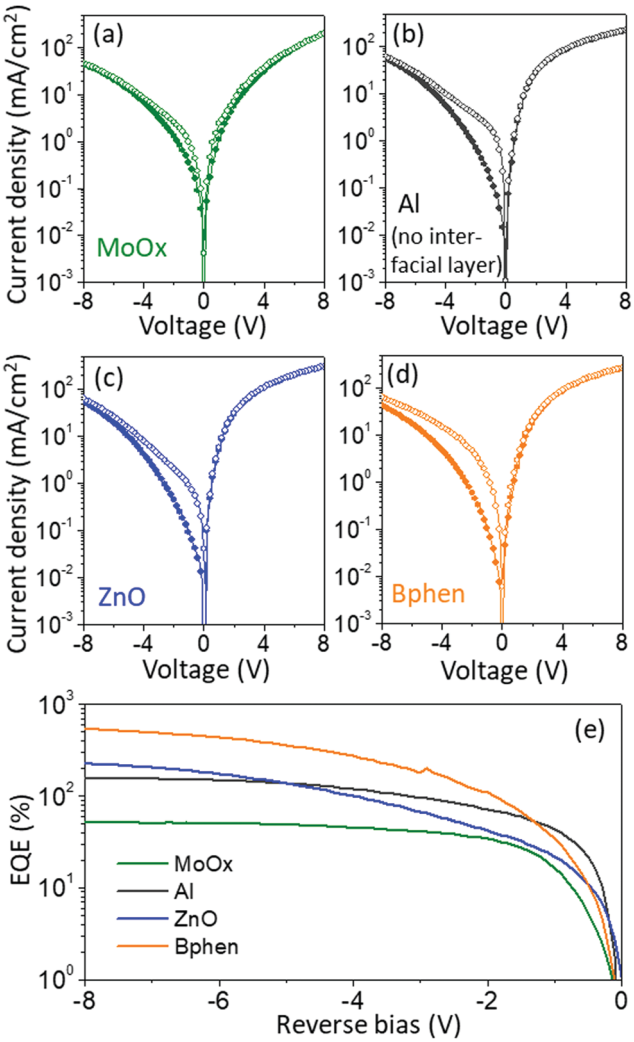

Fig. 2 Current density *versus* applied voltage, measured in the dark (solid symbol) and under illumination (open symbol) of 4.5 mW cm^{-2} from a 1050 nm LED. The interfacial layer was (a) MoOx, (b) not used and the BHJ is in direct contact with the Al electrode, (c) ZnO, and (d) Bphen. (e) External quantum efficiencies of devices with different interfacial layers.

The external quantum efficiency (EQE) in Fig. 2e is calculated by EQE = $(J_{ph}/P_{illumin})(hc/\lambda q)$, where J_{ph} is the photocurrent density obtained from the photoresponse minus the dark current density, $P_{illumin}$ is the intensity of the incident light, h is Planck's constant, c is the speed of light, λ is the wavelength of the incident light, and q is the electron charge. The EQE of the device with MoO_x was at most 52%. On the other hand, the devices with ZnO, Bphen, or direct Al contact achieved EQE above 100%, indicative of photomultiplication.

Since all the devices had identical charge generation layers, it is fair to assume that light absorption and charge generation were the same across these detectors. The difference in photoresponse is attributed to modifications in charge transport and collection processes influenced by the interfacial layer, as illustrated in Fig. 3. In the device with the MoO_x, photogenerated

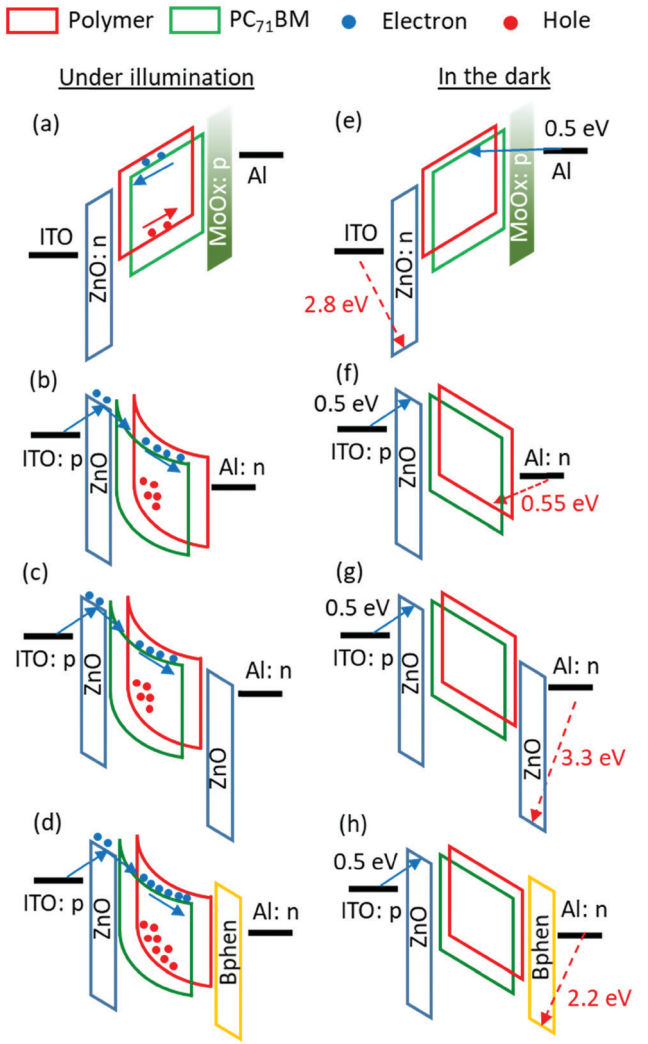

Fig. 3 Energy diagrams of devices with (a and e) MoO_x, (b and f) without an interfacial layer, (c and g) ZnO, and (d and h) Bphen. The devices were under reverse bias. The left column shows the photo-generated charge collection process (a) without and (b–d) with photomultiplication due to hole accumulation, which induced band bending that led to enhanced electron injection. The right column compares charge injection barriers in the dark.

electrons and holes were swept by the applied electric field to the respective ZnO and MoO_x interfaces to be collected (Fig. 3a).

When the MoO_x layer was removed, the work functions of the electrode materials dictated that reverse bias occurred when negative voltage was applied to the ITO electrode. Hole extraction was impeded in the detectors in the absence of MoO_x (direct Al contact) as well as when using ZnO and Bphen interfacial layers. Consequently, photogenerated holes were accumulated in these three detectors. The trapped holes induced band bending, which reduced the barrier for electron injection into the BHJ as indicated in Fig. 3b–d. The injected electrons supplied by the external bias increased the photocurrent. Multiple electrons could be injected per incident photon, resulting in photomultiplication,[15,20] where the charge injection process would continue until the trapped holes recombined.

Comparing the devices with photomultiplication, the EQE was higher in the detector using Bphen than when using ZnO or no interfacial layer. This finding suggests that, compared to the deeper conduction band in ZnO or Al (−4.2 eV), the LUMO level in Bphen (−3.0 eV) prolonged the lifetime of the trapped holes, since the probability of recombination would be lower when there was a larger energy difference between the polymer HOMO (−4.75 eV) and the interface conduction band or LUMO. Non-radiative recombination is a major challenge in organic devices, and non-radiative electron transfer from a higher energy level to the ground state is reduced with wider bandgap.[12] The energy difference of the polymer HOMO and Bphen LUMO is 1.75 eV, while the difference is only 0.5 eV with ZnO and Al interfaces. Therefore the recombination probability is lower for Bphen than the others, benefiting the photomulitiplcation process. Another possibility is that the deposition of Bphen was less damaging to the BHJ surface than Al evaporation or solution coating with ZnO, because Bphen was evaporated at a lower temperature than Al and there was no solvent involved in the vacuum deposition of the Bphen layer.

In addition, we observed that although there is a difference between the valence band of ZnO and the HOMO of Bphen, it did not affect photomultiplication. The photogenerated holes are blocked at the active layer/ZnO interface next to the ITO electrode (Fig. 3b–d). Since the hole blocking effect is not dictated by the Bphen or the ZnO next to the Al electrode, the HOMO level at this interface would not affect the photomultiplication. On the other hand, the difference in LUMO level between the materials changed the recombination probability of the photogenerated carriers as explained in the preceding paragraph.

Effect of the interfacial layer on the dark current

While switching the interfacial materials changed the photoresponse considerably, the device dark current was not significantly affected, as seen in Fig. 4. To explain this result, we examined the charge injection barriers in the detectors. The dark current has contributions arising from multiple mechanisms[31] including charge injection through the electrodes,[23,29] thermal generation in the active layer,[30,32] and frequency dependent noise.[33] The charge injection contribution becomes dominant as the applied bias increased. Charge injection from the electrode into the BHJ is influenced by the characteristics of the interfacial layer, as well as the morphology, energetic landscape, and charge transport properties of the active BHJ layer.[29,34] By first order approximation, the energy difference between the electrode work function and the available energy states in the interfacial materials determined the energy barrier to charge injection Φ_b, independent of the applied field.

Fig. 3e–h illustrates the detectors' energy levels under reverse bias in the dark. For the device with MoO_x, the ITO electrode was next to ZnO, which blocked hole injection. Meanwhile, the Al electrode was interfaced with MoO_x that had energy states near the BHJ LUMOs and which are conducive to electron injection. Thus, charge injection was mainly from the Al/MoO_x side. For the other three devices, all the electrodes

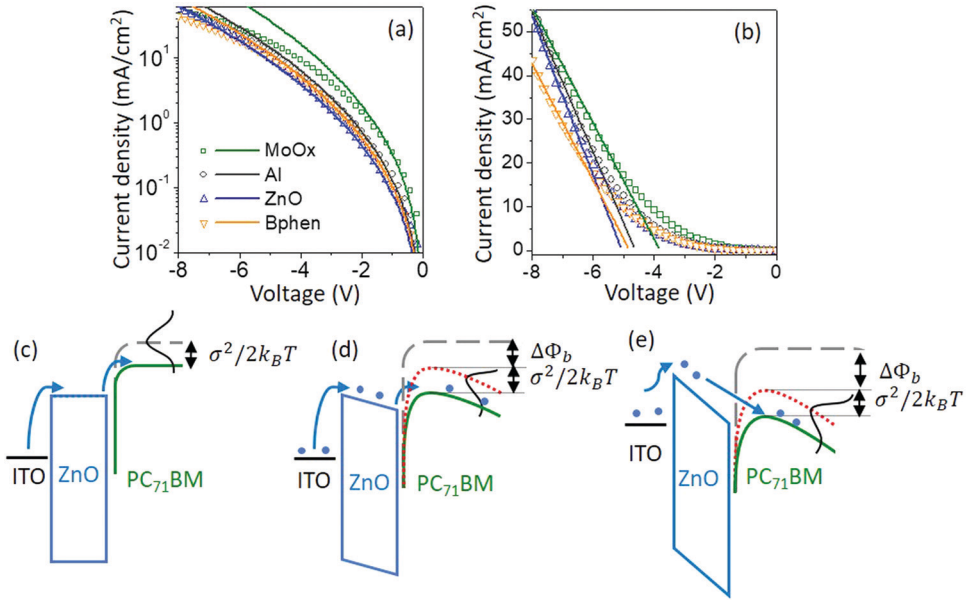

Fig. 4 (a) Current densities of the devices at reverse bias in the dark, with the data represented by open symbols and the lines are fits to eqn (2a). (b) shows the data in a linear scale, and the lines are fits to eqn (2b) in the high electric-field regime. The diagrams illustrate the evolving charge injection barrier at (c) flat band, (d) low electric field, and (e) high electric field. The gray dash line indicates the acceptor LUMO level, the black line represents the Gaussian distribution of energy states, the red dotted line represents the barrier lowering due to the applied electric field, and the solid green line shows the energy level available for charge injection.

were next to materials that were blocking layers to hole injection. The difference between the work function of ITO and the conduction band of ZnO were ~0.5 eV and smaller than the hole injection barriers. Hence, electron injection from the ITO/ZnO side was the determining factor for the dark current in devices with ZnO, Bphen, and direct Al contact. Since this electron injection barrier was the same across these devices, their dark currents were similar as shown in the measurements in Fig. 4.

In addition to the above qualitative explanations, the dark current was analyzed by fitting to the model in ref. 23 to extract charge injection barrier values. According to this model,[23] the field-independent charge injection barrier Φ_b is reduced by the Gaussian distribution of states near the bandtail[35,36] and barrier lowering due to the electric field,[37,38] resulting in an effective charge injection barrier Φ_{inj} described by

$$\Phi_{inj} = \Phi_b - \frac{\sigma^2}{2k_B T} - \sqrt{\frac{qE}{4\pi\varepsilon}}, \quad (1)$$

where the second term $\sigma^2/(2k_BT)$ accounts for the energetic disorder at the interface that increases states for charge injection, and the third term $\Delta\Phi_b = \sqrt{\frac{qE}{4\pi\varepsilon}}$ is the barrier lowering due to the electric field. The parameter σ is the width of the Gaussian distribution, T is the temperature, k_B is Boltzmann's constant, $\varepsilon = \varepsilon_0\varepsilon_r$ is the permittivity where a value of 3.5 was used for ε_r in the calculations, and E is the applied electric field.

The injection limited current density is estimated to be $J_{inj} \sim qn_{inj}\mu E$, where n_{inj} is the carrier density at the injection interface and μ is the effective mobility of the BHJ. The effective mobility is $\mu = \mu_0 \exp\left[-a_i\left(\frac{\sigma}{k_B T}\right)^2\right]$, where μ_0 is the mobility in the infinite temperature limit and $a_i \approx 0.4$ based on ref. 29. The injection model assumes that charge injection occurs at the nearest sites in the active layer adjacent to the interface. In such conditions, the carriers at the top of the barrier have a concentration of $n_{inj} = N_{inj}\exp(-\Phi_{inj}/k_BT)$, where the N_{inj} is the volume density of molecular sites.[29] The equations we used to fit the dark current data in Fig. 4a and b are

$$J_{inj} = qN_{inj}\exp\left(-\frac{\Phi_b - \frac{\sigma^2}{2k_BT} - \sqrt{\frac{qE}{4\pi\varepsilon}}}{k_BT}\right)\mu E; \quad (2a)$$

$$J_{inj} = qN_{inj}\exp\left(-\frac{\Phi_b - \frac{\sigma^2}{2k_BT} - C}{k_BT}\right)\mu(E - E_c), \quad (2b)$$

when $E \geq 5\,\mathrm{V}/200\,\mathrm{nm}$,

where $\Phi_b - C = \Phi_{b,high E}$, and $C = \Phi_{b,max}$ is the maximum extent of electric-field-induced barrier lowering. The fit to eqn (2b) included only data above 5 V to determine $\Phi_{b,high E}$. The factor E_c is the x-intercept in Fig. 4b and indicates the turning point to the high electric-field regime.

In Fig. 4a at low voltage, the measured data were fit using eqn (2a) based on ref. 23, but as the applied bias increased, eqn (2a) led to an over-estimation of the dark current. To improve the fitting, eqn (2b) was used, which assigns $\Delta\Phi_b$ to a maximum constant under high electric fields. The fits based

Table 1 Values obtained from fitting dark current densities to eqn (2). As discussed in the text, $N_{inj} = 10^{27}$ m^{-3}, σ = 50 meV, and $\mu_0 = 10^{-3}$ cm^2 V^{-1} s^{-1}. The error bar is ±1%

Interfacial material	Φ_b (meV)	$\Phi_{b,highE}$ (meV) for $V > 5$ V	$C = \Phi_b - \Phi_{b,highE}$ (meV)
MoO_x	533	372	161
Al	557	367	190
ZnO	570	364	206
Bphen	563	372	191

on eqn (2b) are closely matched to the data at biases above 5 V, as evident in Fig. 4b. The rationale behind this modification is that, as the applied voltage increased to tilt the energy levels (from Fig. 4c and d), $\Delta\Phi_b$ was initially effective at reducing Φ_{inj} (solid green line). However, when the bias reached the point that the barrier between ZnO and $PC_{71}BM$ was overcome (Fig. 4e), any further voltage increase will not affect the injection barrier, and the barrier lowering plateaued and can be treated as a constant $C = \Delta\Phi_{b,max}$ as in eqn (2b). The extracted C in Table 1 are around 200 meV, which is reasonable considering the LUMO difference between ZnO and $PC_{71}BM$, as shown in Fig. 1d.

Table 1 summarizes values obtained in fits to eqn (2). The values of Φ_b are around 0.55 V. This finding confirms that charge injection was mainly from the ITO/ZnO electrode for the devices with photomultiplication, in agreement with the energy offset between ITO and ZnO as shown in Fig. 1. For the device with the MoO_x interface, the MoO_x/Al electrode would be the injection site. Although the energy offset between Al and $PC_{71}BM$ is only 0.3 eV in Fig. 1, the fit value of 0.53 eV is still reasonable, as MoO_x has available states spanning the $PC_{71}BM$ bandgap and also might slightly deepen the Al work function.

Analysis on the highest performance device with the Bphen interface

Among the detectors fabricated in this work, the device with the Bphen interface showed the best performance and was further analyzed with respect to its detectivity, light-intensity dependent photoresponse, and temporal response. The responsivity R, defined as $R = J_{ph}/P_{illum}$, as a function of incident wavelength is shown in Fig. 5a, with a broadband photoresponse from the visible to SWIR covering 600 nm to 1400 nm. The responsivity is related to specific detectivity D^* by

$$D^* = \frac{R\sqrt{A}}{S_n}, \quad (3)$$

where A is the active area of the detector and S_n is the noise current density in A Hz$^{-0.5}$. Specific detectivity is the signal to noise ratio. Here, determination of the noise current was carried out by direct measurement *via* a lock-in amplifier. As S_n varies as a function of frequency, applied bias, and temperature, Fig. 5b is a snapshot of the noise current S_n at an applied bias of −3 V at room temperature. We compared the measured noise to the shot noise based on $S_{n,shot} = \sqrt{2qI_{dark}}$. For example, the dark current for our detector with Bphen was $I_{dark} = 2 \times 10^{-4}$ A at a bias of −3 V; and substituting this into the

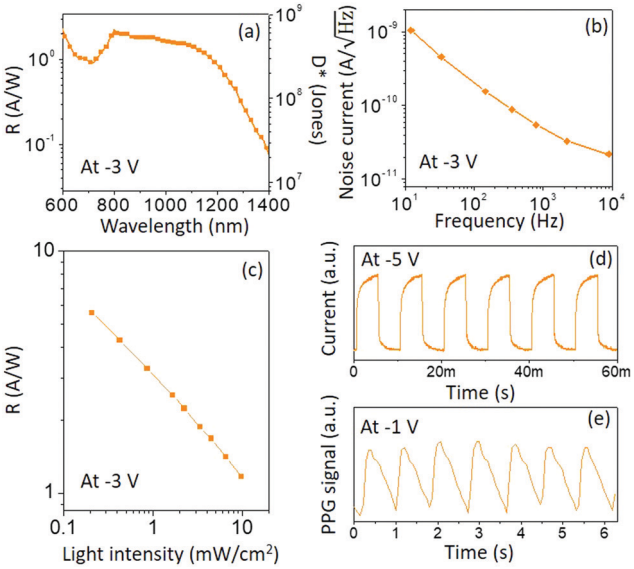

Fig. 5 For the device with Bphen as the interfacial layer, (a) responsivity and specific detectivity as a function of wavelength, recorded at a frequency of 12 Hz, with the incident light intensity of 3 mW cm^{-2} at 1050 nm. (b) Noise current as a function of frequency. (c) Responsivity *versus* light intensity from a LED emitting at the wavelength of 1050 nm. (d) Temporal response under a LED light modulated at 100 Hz. (e) Photoplethysmogram measured at a fingertip to show a person's heart rate. The LED in (d) and (e) emitted at the wavelength of 940 nm. The applied bias on the photodetector is indicated inside each panel.

$S_{n,shot}$ equation, the calculated shot noise was 8×10^{-12} A/$\sqrt{\text{Hz}}$ and lower than the total noise values from the lock-in measurements that include $1/f$ and thermal noise components. Thus, we calculated D^* with the total noise from Fig. 5b. Since the photoresponse was measured at a frequency of 12 Hz, we took the noise current density at this frequency for the calculation of D^*. For a light intensity level around few mW cm^{-2}, the D^* is $<10^9$ Jones (*i.e.*, cm Hz$^{0.5}$ W^{-1}) as shown in the right axis of Fig. 5a. This D^* is lower than previous values reported for photodiodes, due to the higher noise under high applied bias.[13]

However, the D^* would increase with lower incident light intensity, because fewer photogenerated holes would occupy deep trap states. Charges escape slowly from deep traps on account of high activation energies, leading to long lifetimes and high photoconductive gain and responsivity.[39,40] As displayed in Fig. 5c, the responsivity was inversely proportional to the illumination intensity, and the device with Bphen achieved 5.6 A W^{-1} (equivalent EQE = 660%) under a low light intensity of 0.2 mW cm^{-2}, resulting in a D^* of 1.6×10^9 Jones. The comparison of EQE under high and low incident light power emphasized the light-intensity dependent characteristics in photomultiplication devices.

Fig. 5d shows the temporal response of the device with Bphen measured under a LED modulated at 100 Hz. On account of the photomultiplication mechanism, the rise and fall characteristics of the photocurrent were asymmetric. The photocurrent kept rising until an equilibrium was established between hole detrapping/recombination and electron charge

injection. On the other hand, the fall time in this device was ~1 ms, indicating that traps were emptied within this time scale when the incident light was switched off. The rise and fall times involve different processes of establishing trap equilibrium *versus* detrapping, and thus they do not need to be the same. With these temporal characteristics, the device was capable of monitoring heart pulses in a photoplethysmogram system.[41–43] A person's fingertip was placed between a LED light source and the photodetector. The photodetector recorded the light intensity variation with periodic arterial pulses, revealing a heart rate of ~70 beats per minute as shown in Fig. 5e. This demonstration shows the potential of this photomultiplication-based detector for practical applications.

Conclusions

This work has investigated a series of interfacial materials to understand how charge blocking layers facilitate the photomultiplication process in SWIR detectors. By tuning the hole blocking layer, the photogenerated holes are not immediately collected by the electrodes and trapped within BHJs. The accumulation of photogenerated holes at the interface lead to band bending, which lowers the electron injection barrier and allows multiple electrons to be injected per photon absorbed, resulting in photomultiplicative gain.

This work has also studied the effect of interfacial layers on the device dark current. Under reverse bias, the dark current at low voltage is accurately described by relating it to a charge injection barrier dependent on the electric field. However, as the applied voltage increases, the barrier becomes independent of the electric field, because the electric-field-induced barrier lowering effect has plateaued.

Among the interfaces studied in this work, the best detectivity is observed in the device with the interfacial layer Bphen, which reduces recombination probability and extends the lifetime of trapped holes to increase photomultiplication. At a low illumination intensity of 0.2 mW cm^{-2}, the photodetector with Bphen achieved a responsivity of 5.6 A W^{-1} (equivalent EQE = 661% at 1050 nm) and a detectivity up to 1.6×10^9 Jones with a broadband photoresponse from 600 nm to 1400 nm. By comparing interfacial materials with different HOMO–LUMO levels, this work presents guidelines to design organic SWIR detectors with energy levels that enable photomultiplication and provides insights into the characteristics of injection barriers affecting the dark current and detectivity.

Conflicts of interest

The authors declare no competing financial interest.

Acknowledgements

The authors N. L. and T. N. N. are grateful for the support from National Science Foundation (ECCS-1839361) and Samsung Advanced Institute of Technology. The work performed at The University of Southern Mississippi was made possible through the Air Force Office of Scientific Research under the support provided by the Organic Materials Chemistry Program (FA9550-17-1-0261) and was supported by the National Science Foundation (OIA-1757220).

References

1 A. Rogalski, *Proc. SPIE 10433*, 2017, p. 104330L.
2 H. Liu, G. Hong, Z. Luo, J. Chen, J. Chang, M. Gong, H. He, J. Yang, X. Yuan, L. Li, X. Mu, J. Wang, W. Mi, J. Luo, J. Xie and X. D. Zhang, *Adv. Mater.*, 2019, **31**, 1901015.
3 O. T. Bruns, T. S. Bischof, D. K. Harris, D. Franke, Y. Shi, L. Riedemann, A. Bartelt, F. B. Jaworski, J. A. Carr, C. J. Rowlands, M. W. B. Wilson, O. Chen, H. Wei, G. W. Hwang, D. M. Montana, I. Coropceanu, O. B. Achorn, J. Kloepper, J. Heeren, P. T. C. So, D. Fukumura, K. F. Jensen, R. K. Jain and M. G. Bawendi, *Nat. Biomed. Eng.*, 2017, **1**, 0056.
4 J. A. Carr, D. Franke, J. R. Caram, C. F. Perkinson, M. Saif, V. Askoxylakis, M. Datta, D. Fukumura, R. K. Jain, M. G. Bawendi and O. T. Bruns, *Proc. Natl. Acad. Sci. U. S. A.*, 2018, **115**, 4465.
5 G. Hong, S. Diao, J. Chang, A. L. Antaris, C. Chen, B. Zhang, S. Zhao, D. N. Atochin, P. L. Huang, K. I. Andreasson, C. J. Kuo and H. Dai, *Nat. Photonics*, 2014, **8**, 723–730.
6 Z. Wu, Y. Zhai, H. Kim, J. D. Azoulay and T. N. Ng, *Acc. Chem. Res.*, 2018, **51**, 3144–3153.
7 Q. Li, Y. Guo and Y. Liu, *Chem. Mater.*, 2019, **31**, 6359–6379.
8 N. Li, Z. Lan, L. Cai and F. Zhu, *J. Mater. Chem. C*, 2019, **7**, 3711–3729.
9 C. Wang, X. Zhang and W. Hu, *Chem. Soc. Rev.*, 2020, **49**, 653–670.
10 I. Constantinou, X. Yi, N. T. Shewmon, E. D. Klump, C. Peng, S. Garakyaraghi, C. K. Lo, J. R. Reynolds, F. N. Castellano and F. So, *Adv. Energy Mater.*, 2017, **7**, 1601947.
11 Z. Wu, Y. Zhai, W. Yao, N. Eedugurala, S. Zhang, L. Huang, X. Gu, J. D. Azoulay and T. N. Ng, *Adv. Funct. Mater.*, 2018, **28**, 1805738.
12 J. Benduhn, K. Tvingstedt, F. Piersimoni, S. Ullbrich, Y. Fan, M. Tropiano, K. A. McGarry, O. Zeika, M. K. Riede, C. J. Douglas, S. Barlow, S. R. Marder, D. Neher, D. Spoltore and K. Vandewal, *Nat. Energy*, 2017, **2**, 17053.
13 Z. Wu, W. Yao, A. E. London, J. D. Azoulay and T. N. Ng, *Adv. Funct. Mater.*, 2018, **28**, 1800391.
14 Y. Wu, K. Fukuda, T. Yokota and T. Someya, *Adv. Mater.*, 2019, 1903687.
15 W. Wang, F. Zhang, M. Du, L. Li, M. Zhang, K. Wang, Y. Wang, B. Hu, Y. Fang and J. Huang, *Nano Lett.*, 2017, **17**, 1995–2002.
16 L. Li, F. Zhang, J. Wang, Q. An, Q. Sun, W. Wang, J. Zhang and F. Teng, *Sci. Rep.*, 2015, **5**, 9181.
17 M. S. Jang, S. Yoon, K. M. Sim, J. Cho and D. S. Chung, *J. Phys. Chem. Lett.*, 2018, **9**, 8–12.
18 M. Hiramoto, T. Imahigashi and M. Yokoyama, *Appl. Phys. Lett.*, 1994, **64**, 187–189.

19 J. Han, D. Yang, D. Ma, W. Qiao and Z. Y. Wang, *Adv. Opt. Mater.*, 2018, **6**, 1800038.
20 J. Miao and F. Zhang, *Laser and Photonics Reviews*, 2019, **13**, 1800204.
21 Z. Zhao, J. Wang, C. Xu, K. Yang, F. Zhao, K. Wang, X. Zhang and F. Zhang, *J. Phys. Chem. Lett.*, 2020, **11**, 366–373.
22 D. Guo, D. Yang, J. Zhao, A. Vadim and D. Ma, *J. Mater. Chem. C*, 2020, 9024–9031.
23 G. Simone, M. J. Dyson, S. C. J. J. Meskers, R. A. J. J. Janssen and G. H. Gelinck, *Adv. Funct. Mater.*, 2019, 1904205.
24 P. Schulz, S. R. Cowan, Z. L. Guan, A. Garcia, D. C. Olson and A. Kahn, *Adv. Funct. Mater.*, 2014, **24**, 701–706.
25 J. Meyer, S. Hamwi, M. Kröger, W. Kowalsky, T. Riedl and A. Kahn, *Adv. Mater.*, 2012, **24**, 5408–5427.
26 A. London, L. Huang, B. Zhang, B. Oviedo, J. Tropp, W. Yao, Z. Wu, B. Wong, T. N. Ng and J. D. Azoulay, *Polym. Chem.*, 2017, **8**, 2922–2930.
27 B. S. Ong, C. Li, Y. Li, Y. Wu and R. Loutfy, *J. Am. Chem. Soc.*, 2007, **129**, 2750–2751.
28 W. J. E. Beek, M. M. Wienk and R. A. J. Janssen, *Adv. Funct. Mater.*, 2006, **16**, 1112–1116.
29 G. Simone, M. J. Dyson, C. H. L. Weijtens, S. C. J. Meskers, R. Coehoorn, R. A. J. Janssen and G. H. Gelinck, *Adv. Opt. Mater.*, 2019, 1901568.
30 Z. Wu, N. Li, N. Eedugurala, J. D. Azoulay, D.-S. Leem and T. N. Ng, *npj Flexible Electronics*, 2020, **4**, 6.
31 Y. Fang, A. Armin, P. Meredith and J. Huang, *Nat. Photonics*, 2019, **13**, 1–4.
32 H. Shekhar, O. Solomeshch, D. Liraz and N. Tessler, *Appl. Phys. Lett.*, 2017, **111**, 223301.
33 H. Katsu, Y. Kawasugi, R. Yamada and H. Tada, 2011 21st International Conference on Noise and Fluctuations, 2011, 77–79.
34 P. E. Keivanidis, P. K. H. Ho, R. H. Friend and N. C. Greenham, *Adv. Funct. Mater.*, 2010, **20**, 3895–3903.
35 J. J. M. Van Der Holst, M. A. Uijttewaal, R. Balasubramanian, R. Coehoorn, P. A. Bobbert, G. A. De Wijs and R. A. De Groot, *Phys. Rev. B: Condens. Matter Mater. Phys.*, 2009, **79**, 085203.
36 W. F. Pasveer, J. Cottaar, C. Tanase, R. Coehoorn, P. A. Bobbert, P. W. M. Blom, M. De Leeuw and M. A. J. Michels, *Phys. Rev. Lett.*, 2005, **94**, 206601.
37 V. I. Arkhipov, U. Wolf and H. Bässler, *Phys. Rev. B: Condens. Matter Mater. Phys.*, 1999, **59**, 7514–7520.
38 J. C. Scott and G. G. Malliaras, *Chem. Phys. Lett.*, 1999, **299**, 115–119.
39 H. Kim, Z. Wu, N. Eedugurala, J. D. Azoulay and T. N. Ng, *ACS Appl. Mater. Interfaces*, 2019, **11**, 36880–36885.
40 Y. S. Rim, Y. M. Yang, S. Bae, H. Chen, C. Li, M. S. Goorsky and Y. Yang, *Adv. Mater.*, 2015, **27**, 6885–6891.
41 Y. Khan, A. E. Ostfeld, C. M. Lochner, A. Pierre and A. C. Arias, *Adv. Mater.*, 2016, **28**, 4373–4395.
42 J. Huang, J. Lee, J. Vollbrecht, V. V. Brus, A. L. Dixon, D. X. Cao, Z. Zhu, Z. Du, H. Wang, K. Cho, G. C. Bazan and T. Q. Nguyen, *Adv. Mater.*, 2020, **32**, 1906027.
43 N. Li, Z. Lan, Y. S. Lau, J. Xie, D. Zhao and F. Zhu, *Adv. Sci.*, 2020, 2000444.

